Crystal Orientation Imaging of Organic Monolayer Islands by Polarized Light Microscopy

Hattori, Yoshiaki

Kitamura, Masatoshi

(Citation)
ACS Applied Materials & Interfaces,12(32):36428-36436

(Issue Date)
2020-08-12

(Resource Type)
journal article

(Version)
Accepted Manuscript

Crystal orientation imaging of organic monolayer islands by polarized light microscopy

Yoshiaki Hattori[†*] *and Masatoshi Kitamura*[†*]

[†]Department of Electrical and Electronic Engineering, Kobe University, 1-1, Rokkodai-cho, Nada, Kobe, 657-8501, Japan

*Corresponding Author:

hattori@eedept.kobe-u.ac.jp (Y. Hattori), kitamura@eedept.kobe-u.ac.jp (M. Kitamura)

ABSTRACT: The initial stage of organic semiconductor film formation greatly affects the properties of films, which are used in organic devices including thin-film transistors and light-emitting diodes. Organic monolayer islands that are formed on a suitable substrate can be observed with a conventional optical microscope. Furthermore, the use of a polarized microscope allows to determine the refractive index and crystal orientation of islands. Here, we report organic monolayer islands of 2,9-diphenyl-dinaphtho[2,3-*b*:2′,3′-*f*]thieno[3,2-*b*]thiophene (DPh-DNTT) deposited on a Si substrate with thermally grown SiO_2 to investigate the crystal orientation of islands by polarized light microscopy. The observation of DPh-DNTT islands under polarized quasi-monochromatic light reveals that reflection intensity depends on both the crystal orientation and irradiation wavelength. A comparison between experimental and calculated reflection intensities provides an estimate of an anisotropic complex refractive index in the plane. The crossed-polarized microscopy image of a SiO_2/Si substrate with DPh-DNTT islands shows that the contrast between the islands and SiO_2 surface is sensitive to the angle between the polarizer and analyzer and depends on the direction of crystal orientation. The dependence of reflection contrast, which can be explained by the anisotropic extinction coefficient, is used to confirm crystal orientation.

KEYWORDS: DPh-DNTT, 2D island, crystal orientation, polarized light microcopy, anisotropic refractive index

INTRODUCTION

The quality of an organic film considerably affects the performance of electronic devices in which the organic film is used as a semiconductor layer. Therefore, the characterization of organic films is an important issue for the realization of good electronic devices and for the preparation of ideal films. In organic films, the anisotropic carrier mobility[1–4] and/or the presence of grain boundaries[5, 6] mainly characterize the carrier transport in the film. Thus, to examine the effect on device performance, it is necessary to confirm the crystal orientation of organic films. The confirmation of crystal orientation in bulk or thin-films was performed by X-ray diffraction,[3, 7–16] low-energy electron diffraction (LEED),[17–19] photoemission electron microscopy,[20] optical measurements,[2, 14–16, 21–38] and atomic force microscopy (AFM).[2, 30, 39–43] For small molecule organic materials that are soluble in organic solvents, X-ray diffraction measurement and absorption spectroscopy[2, 15, 16, 21, 22] have been used to investigate crystal orientation in relative large single-crystal thin films, which were prepared by the edge-casting method.[2, 23, 33] However, the preparation of thin films composed of insoluble organic materials is currently limited to vacuum deposition, which produces polycrystalline thin films. To investigate these polycrystalline organic thin films, a spatially resolved microscopic measurement[2, 14, 15, 17–19, 24–43] is useful to reveal the orientation of individual grains in the polycrystalline film. The crystal orientation of organic polycrystalline thin films has been investigated by microbeam LEED[17–19] and atomic force microscopy in transvers shear microscopy (TSM) in AFM measurements,[2, 30, 39–43] which require to perform measurements in vacuum and/or long-time measurements. Currently, fast and simple techniques are needed to investigate the microstructure, including crystal orientation, of organic thin films over a large area on a substrate surface.

Polarized light microscopy (PLM) has been used to evaluate the crystallinity of organic thin films.[2, 15, 27, 30–38, 44, 45] The microscopy can quickly image crystal domains with sub-micrometer resolution in cross-polarized observation for which two polarizers are used. This occurs because the observed color of a crystal domain depends on the crystal orientation. However, crystal domains observed in the same color do not always have the same orientation. This means that usual observation does not completely identify the crystal axes in the polycrystalline film. To overcome this disadvantage, a waveplate or a Nomarski prism is additionally inserted into the optical pass of a microscope for identification.[31, 46] However, a

reduction in the film thickness suppresses the visibility of crystal domains and the color contrast among crystal domains with different orientations even when using an additional optical component. Thus, few studies have been conducted to evaluate the orientation of organic films with a thickness of a few nanometers by PLM.

In this study, we measure refractive index and determine crystal orientation in monolayer-thick organic two-dimensional islands of 2,9-diphenyl-dinaphtho[2,3-*b*:2′,3′-*f*]thieno[3,2-*b*]thiophene (DPh-DNTT) that are formed on a silicon substrate with thermally grown SiO_2. DPh-DNTT is a promising material for organic thin-film transistors; it has high thermal stability compared with other organic semiconductors. We observed DPh-DNTT islands using a standard reflected light microscope with two polarizers without an additional component such as a waveplate or a Nomarski prism. The anisotropic optical absorption in DPh-DNTT islands allows to confirm crystal orientation. The use of a narrow band-pass filter and adjustment of the polarizer angle enhance luminance contrast difference among islands with different orientations. When DPh-DNTT with a nominal sub-monolayer thickness is deposited on a substrate, monolayer-thick DPh-DNTT islands are randomly formed on the substrate surface. We focus on the observation of DPh-DNTT islands under polarized quasi-monochromatic illumination. The dependence of reflected light luminance on crystal orientation and wavelength are statistically investigated by analyzing many islands. The anisotropic refractive index is estimated by comparing measured values with those calculated by an analytical formula. Furthermore, we introduce a method to enhance the visibility of crystal orientation using two polarizers.

RESULTS AND DISCUSSION

Optical analysis model of DPh-DNTT islands

Organic monolayer islands grown on a substrate can be observed with an optical microscope despite their thickness of approximately 2.3 nm.[47–49] The justification of the thickness is described in the method. **Figure 1a** shows a dark-field optical microscope image of typical DPh-DNTT islands grown on a silicon substrate with a SiO_2 layer examined in this study.

The color is inverted from the original color to emphasize the boundary of the island. The islands with a cruciform shape and long and short axes are randomly arranged on the substrate. **Figure 1b** shows a schematic illustration of a DPh-DNTT island. When the horizontal and vertical directions of a microscope image are, respectively, defined as *x*- and *y*-axes, the direction of an island is identified by the angle of the long axis to the *x*-axis (θ), as shown in **Fig. 1b**.

The cruciform shape of the DPh-DNTT island seen in **Fig. 1a** almost has two lines of symmetry, which seems to reflect the crystal axis of the island that DPh-DNTT molecules are positioned perpendicular to the substrate and are periodically arranged. An X-ray diffraction study has shown that a bulk crystal of DPh-DNTT molecules has a monoclinic structure with unit cells consisting of two DPh-DNTT molecules stacked in a herringbone structure.[8] **Figure 1c** shows the molecular structure of DPh-DNTT and the top-view illustration of the herringbone structure. The *a*- and *b*-axes of the plane on which molecules stand form 90° in the monoclinic structure. Because the long and short axes of a cruciform DPh-DNTT island are orthogonal, these axes may correspond to *b*- and *a*-axes of the crystal structure. The correspondence is explained in "Assignment of long and short axes" section.

A bright-field microscope image reflects the thickness and optical properties of organic monolayer islands. Although a dark-field observation clearly shows island boundary, the observed image hardly contains information of island thickness and optical properties, as seen in **Fig. 1a**. **Figure 1d** shows the schematic illustration of an optical microscope used in this study. The microscope has a polarizer for incident light and an analyzer for reflected light; the polarizer is rotatable. The transmission axes for the polarizer and the analyzer are represented by angles α_1 and α_2, respectively, which are defined as angles to the *x*-axis. In this study, the analyzer is fixed at $\alpha_2 = 90°$. Narrow band-pass filters with band centers of different wavelengths (λ) were used to realize a quasi-monochromatic illumination. The difference between the reflected light intensity from an SiO_2 surface (I_{sub}) and that from a DPh-DNTT island (I_{DNTT}) allows us to visualize the island in the microscope image. To quantitatively evaluate the degree of visualization, the luminance contrast of an island (C_{exp}) in a microscope image is defined as

$$C_{exp} = \frac{D_{DNTT} - D_{sub}}{D_{sub}} \tag{1}$$

where D_x (x = DNTT or sub) is a digital value calculated from the microscope image captured with a digital camera. The subscript DNTT and sub represent digital values obtained from the areas of the DPh-DNTT island and SiO_2 surface. The digital values of $D_x = 0$ and 255 correspond to black and white colors, respectively. In the definition, an island with $C_{exp} > 0$ ($-1 \leq C_{exp} < 0$) is brighter (darker) than a substrate. Large $|C_{exp}|$ provides high island visibility in the image. The $|C_{exp}|$ values depend on θ, α_1, α_2, λ, and on whether the analyzer is inserted. The details of the image analysis procedure are described in the Supporting Information.

The luminance contrast C_{exp} calculated from a microscope image corresponds to the intensity contrast (C_{cal}) represented by the following expression:

$$C_{cal} = \frac{I_{DNTT} - I_{sub}}{I_{sub}} \tag{2}$$

The expression of intensities I_{DNTT} and I_{sub} can be derived from an optical model for a DPh-DNTT island grown on a SiO_2/Si substrate shown in **Fig. 1e**. Although we assume that light is vertically incident in this study, the optical path is represented by an angled arrow to avoid the overlap of arrows. By substituting the equations of I_{DNTT} and I_{sub} into **Eq. (2)**, analytical intensity contrast (C_{cal}) can be obtained as a function of θ and α_1. The detailed derivation is described in the Supporting Information.

When a DPh-DNTT island is observed by an incident light polarized at $\alpha_1 = 0°$ without an analyzer, C_{cal} is written as

$$C_{cal} = \frac{1}{2}\left(\left|\frac{r_L}{r_{sub}}\right|^2 - \left|\frac{r_S}{r_{sub}}\right|^2\right)\cos 2\theta + \frac{1}{2}\left(\left|\frac{r_L}{r_{sub}}\right|^2 + \left|\frac{r_S}{r_{sub}}\right|^2 - 2\right) \tag{3a}$$

$$= A_1 \cos 2\theta + A_2 \tag{3b}$$

where A_1 and A_2 are defined as real-value functions of reflection coefficients: r_L, r_S, and r_{sub}. r_L and r_S are the complex-value functions, containing complex refractive indices N_{1L} and N_{1S}. These reflection coefficients and complex refractive indices are defined in the optical model. When $N_{1L} \neq N_{1S}$, r_L is not equal to r_S, and C_{cal} depends on θ with a period of 180°.

When a DPh-DNTT island is observed by an incident light polarized at $\alpha_1 \neq 0°$ through an analyzer of $\alpha_2 = 90°$, C_{cal} is written as

$$C_{cal} = \left| \frac{r_L}{r_{sub}} \frac{\cos\theta \sin(\theta - \alpha_1)}{\sin\alpha_1} - \frac{r_S}{r_{sub}} \frac{\sin\theta \cos(\theta - \alpha_1)}{\sin\alpha_1} \right|^2 - 1 \tag{4a}$$

$$= B_1 \left(\frac{\sin\theta \cos(\theta - \alpha_1)}{\sin\alpha_1} \right)^2 + B_2 \left(\frac{\cos\theta \sin(\theta - \alpha_1)}{\sin\alpha_1} \right)^2 - B_3 \left(\frac{\sin\theta \cos(\theta - \alpha_1)}{\sin\alpha_1} \right) \left(\frac{\cos\theta \sin(\theta - \alpha_1)}{\sin\alpha_1} \right) - 1 \tag{4b},$$

where B_1, B_2, and B_3 are real constants. When $\alpha_1 = 0°$ and $\alpha_2 = 90°$, $I_{sub} = 0$ and C_{cal} is infinite. Thus, C_{exp} is compared with I_{DNTT}. In this case, I_{DNTT} is expressed by

$$I_{DNTT} = \frac{E_i^2}{4} |r_L - r_S|^2 (1 - \cos 4\theta) = F(1 - \cos 4\theta) \tag{5}$$

where F is the real constant, which exhibits four periods in 360° rotation. Although the light reflected from the SiO_2 surface of an incident light of $\alpha_1 = 0°$ ideally does not pass through the analyzer of $\alpha_2 = 90°$, D_{sub} experimentally does not equal zero. Because D_{sub} for $\alpha_1 = 0°$ is extremely small compared to D_{sub} for $\alpha_1 \neq 0°$, the observation at $\alpha_1 = 0°$ enhances the color contrast of DPh-DNTT islands. Experimental C_{exp} values are discussed on the basis of **Eqs. (3)−(5)** depending on θ.

Refractive index determination by observation without an analyzer

Figure 2a shows a dark-field microscope image of DPh-DNTT islands grown on a SiO_2/Si substrate treated with an HF solution. The boundary of the DPh-DNTT island with monolayer steps is clearly seen as a bright color. Because the long and short axes of an island can be specified, we can define θ for the island. **Figure 2b** shows a microscope image of the same area as in **Fig. 2a** in the bright field acquired using the polarizer of $\alpha_1 = 0°$ without an analyzer. The substrate was irradiated through a narrow band-pass filter with a band center at 498 nm. The double arrow in the image indicates the transmission axis of the polarizer. In **Fig.**

2a, an island labeled with "a" has θ close to 0°. These islands are almost invisible in **Fig. 2b**. However, the island labeled with "b" has θ close to 90°. These islands are darker than the surrounding area in **Fig. 2b**. We calculated C_{exp} defined in **Eq. (1)** for islands on the same substrate as **Fig. 2b** to quantitatively evaluate visibility. **Figure 2c** shows C_{exp} versus θ as closed circles for more than 170 islands. C_{exp} has a period of $\theta = 180°$ and is symmetric at $\theta = 90°$. The solid line in **Fig. 2c** shows a fitting curve to closed circles obtained using **Eq. (3)** by the least squares method. The agreement between the closed circles and the solid line confirms that the C_{exp} versus θ characteristics can be explained by **Eq. (3)**. Because C_{cal} depends on θ under the condition of $|r_L| \neq |r_S|$, the dependence of C_{exp} on θ indicates that the DPh-DNTT island is an optical anisotropic material. The fitting to C_{exp} determines A_1 and A_2 in **Eq. 3b**, i.e., $|r_L|$ and $|r_S|$ at the chosen wavelength, respectively. If the complex refractive index and the thickness of each layer are determined, C_{exp} can be calculated. Conversely, the real and imaginary parts of N_{1L} (N_{1S}) cannot be independently determined from the $|r_L|$ ($|r_S|$) value obtained at a certain wavelength even if other parameters except for N_{1L} (N_{1S}) are known. Therefore, we examined the dependence of C_{exp} on the wavelength.

The analysis of C_{exp} at multiple wavelengths allows us to estimate N_{1L} and N_{1S}, which in this study are assumed to have no dispersion.[50, 51]. When $\theta = 0°$, C_{cal} is expressed as

$$C_{cal} = |r_L|^2/|r_{sub}|^2 - 1 \quad (6a)$$

and does not depend on $|r_S|$. When $\theta = 90°$, C_{cal} is expressed as

$$C_{cal} = |r_S|^2/|r_{sub}|^2 - 1 \quad (6b)$$

and does not depend on $|r_L|$. Thus, we can independently estimate N_{1L} in $|r_L|$ and N_{1S} in $|r_S|$ using **Eqs. (6a) and (6b)**, respectively. This is possible because unknown parameters in $|r_L|/|r_{sub}|$ and $|r_S|/|r_{sub}|$ are only N_{1L} and N_{1S}, respectively (see Note S2 of the Supporting Information). The C_{exp} values at some wavelengths are shown as red closed circles for $\theta = 0°$ and as blue closed circles for $\theta = 90°$ in **Fig. 2d**, which are the values at $\theta = 0°$ and $\theta = 90°$ of the fitting curves obtained at the chosen wavelength. The solid line in **Fig. 2d** is a curve fitting of red or blue closed circles performed using **Eqs. (6a) or (6b)**. We obtained $N_{1L} = 1.45(\pm0.05) + 0.2i(\pm0.05i)$ for $\theta = 0°$ and $N_{1S} = 1.45(\pm0.05) + 0.4i$ $(\pm0.05i)$ for $\theta = 90°$ by the fitting. Because C_{cal} is sensitive to n_{1X} and

k_{1X} for N_{1X} (X = L or S), both values can be independently determined by the fitting (**Fig. S2**). Although N_{1L} and N_{1S} have the same value, the k_{1S} value is larger than that of k_{1L}, which indicates that the island exhibits higher absorption for light polarized to the short axis than to long axis. Thus, the dependence on θ in the observation without an analyzer seen in **Fig. 2c** is attributed to the anisotropic absorption of light rather than to the refractive index.

Not all plots obtained from the dependence of C_{exp} on θ are close to the fitting curve over the entire wavelength range in **Fig. 2d**. The difference between the plot and the fitting curve increases at wavelengths above 600 nm. In addition, the difference is also large at the wavelength of 498 nm, which is close to the absorption edge of the DPh-DNTT film predicted from the energy band gap of 2.6 eV.[52] The difference may be due to the assumption that, in this study, the refractive index of DPh-DNTT is independent of the wavelength. When determining crystal axis, the anisotropic absorption is more important than the dispersion of the refractive index. Therefore, we used the complex refractive index shown above for the determination of crystal axis.

The refractive index of a layer is typically examined by ellipsometry. In fact, the refractive indices for a pentacene polycrystalline thin-film have been reported.[53–55] Although pentacene is a standard material for organic thin-film transistors, the measured dispersion of refractive index varies in the reports. This indicates difficulty in measuring the refractive index of organic thin films.

Orientation determination by observation with an analyzer

Figure 3 shows the bright-field microscope images of the same area as in **Figs. 2a and 2b**, acquired using a polarizer of α_1 = 5°, 0°, and −5° and an analyzer. The substrate was irradiated through a narrow band-pass filter with a band center of 498 nm. The double arrows labeled with "P" and "A" in the images indicate the transmission axes of the polarizer and analyzer, respectively. For α_1 = 0°, the islands with $\theta \sim 45°$ or 135° are imaged as bright color, as seen in **Fig. 3b**. Brightness can be explained using **Eq. (5)**. In this case, α_1 = 0° and α_2 = 90°, I_{DNTT} has a maximum at $\theta = 45° + 90° j$ (j : integer). This is a typical characteristic observed in

PLM of $\alpha_2 - \alpha_1 = 90°$ in which the brightness changes with a period of $\theta = 90°$. However, the periodicity of brightness for $\alpha_1 = 5°$ or $-5°$ differs from that for $\alpha_1 = 0°$. DPh-DNTT islands in bright and dark colors are seen in **Figs. 3a and 3c**. For $\alpha_1 = 5°$, the islands with $\theta \sim 45°$ and 135° are shown as bright and dark colors, respectively. For $\alpha_1 = -5°$, the island with $\theta \sim 45°$ and 135° appear as dark and bright colors, respectively. The brightness and darkness change with a period of $\theta = 180°$ according to **Eq. (4)**. The dependence of brightness and darkness on θ has not been observed in the conventional PLM of $\alpha_2 - \alpha_1 = 90°$ for organic thin films.[34, 37]

Figure 4a shows the C_{exp} values for $\alpha_1 = 5°$, 0°, and $-5°$ depending on θ for **Fig. 3**. For $\alpha_1 = 0°$, C_{exp} is high at approximately $\theta = 45°$ and 135°, as a diagonal position, and close to 0 at approximately $\theta = 0°$, 90°, and 180°, as an extinction position. For $\alpha_1 = 5°$, C_{exp} is positive in the range of $0° < \theta < 90°$ and high at approximately $\theta = 45°$, negative in the range of $90° < \theta < 180°$, and close to 0 at approximately $\theta = 0°$, 90°, and 180°. For $\alpha_1 = -5°$, the dependence of C_{exp} on θ is symmetric with respect to that for $\alpha_1 = 5°$ at $\theta = 90°$. The solid line in **Fig. 4a** is a curve fitting of black, red, or blue closed circles using **Eqs. 4 or 5**, which are obtained by the least squares method. For each α_1, the closed circles are close to the fitting curve. The agreement between the experimental data and the fitting curve supports that the analytical model expressed by **Eqs. 4 and 5** is valid and can explain the observation of organic molecular islands by PLM. Consequently, bright and dark islands are attributed to the anisotropic refractive index of DPh-DNTT.

The value of $|C_{exp}|$ in **Figs. 2c or 4a** indicates the degree of visibility of islands with respect to the SiO_2 surface. On the other hand, C_{exp}, which depends on θ, provides the visibility of islands with different orientations. For **Fig. 2c**, the difference in C_{exp} between 0.176 at $\theta = 0°$ and 0.0212 at $\theta = 90°$ is 0.155. The orientation-dependence of luminance is visualized by the difference. In **Fig. 4a**, the difference between C_{exp} at $\theta = 45°$ and that at $\theta = 135°$ is 1.12, which is more than 7 times larger than that for **Fig. 2a**. This result suggests that the visibility of orientation is enhanced using an analyzer and that we can determine the orientation of island from the contrast in the image.

The difference between maximum and minimum C_{exp} values depends on α_1 and λ. Thus, we investigated the dependence in detail. The orange and green plots in **Fig. 4b** show the

experimental contrast as a function of α_1 for λ = 498 nm at θ = 45° and 135°, respectively. The plot at a certain α_1 in **Fig. 4b** was extracted from a curve fitting of plots of C_{exp} as a function of θ such as **Fig. 4a**. The contrast at α_1 = ±90° ideally corresponds to the observation without an analyzer (**Fig. S4**). $|C_{exp}|$ increases as α_1 approaches zero, which enhances the visibility of the islands. While, the visibility of orientation is evaluated by the difference in contrast for θ = 45° and 135° in **Fig. 4b**. Thus, as seen in **Fig. 4b**, the visibility of orientation is very sensitive to α_1 when α_1 is close to zero. The orange and green lines in the figure are drawn on the basis of analytical solutions calculated using the obtained N_{1L} and N_{1S} of DPh-DNTT. The fitting line is not far from the plots, which confirms the validity of the extracted refractive index of DPh-DNTT. The line sharply changes at approximately α_1 = 0°. Theoretically, the difference in contrasts for θ = 45° and 135° is maximum at $|\alpha_1|$ = 1.3°. This means that the visibility of orientation is maximum at $|\alpha_1|$ = 1.3°. Experimentally, we observed the maximum visibility at α_1 = ±5°. Thus, we investigated the wavelength dependence for the visibility at α_1 = −5°.

Figure 4c shows the difference of contrast at θ = 45° and that at θ = 135° depending on the wavelength. The plots show an experimental contrast difference, and the solid line shows the contrast difference calculated using **Eq. 4**. The gray arrow in **Fig. 4c** corresponds to that in **Fig. 4b** and indicates a difference in the contract on the basis of two lines in **Fig. 4b**. Both the experimental and calculated results indicate that orientation visibility is large at approximately 500 nm, which suggests that the wavelength is suitable for orientation imaging. The wavelength at which contrast difference is maximum depends on the thickness of SiO_2 (**Fig. S5a**). For example, orientation visibility exhibits the maximum at 610 nm when the SiO_2 layer has a thickness of 110 nm. According to the calculation, the optimal wavelength and the SiO_2 thickness for the observation are close to those for the observation without polarizers, i.e., normal bright-field image observation (**Fig. S5b**). It is useful to predict the optimal condition in the cross-polarized observation by calculating contrast using a simple model, which has been reported in previous studies.[50, 51]

The dependence of C_{exp} on θ is useful for determining the crystal orientation of DPh-DNTT islands. The method of orientation determination adopted in this study is explained in **Figs. S6 and S7**. We applied the method for round islands in which long and short axes are unclear. **Figure 5a** shows a dark-field optical microscope image of round DPh-DNTT islands

formed on the SiO_2 surface treated with UV-O_3. The red and blue lines in the figure indicate long and short (or *b* and *a*) axes determined by this method, respectively. Additional information about this method is described in the captions of **Figs. S6 and S7**. **Figure 5b** shows the bright-field cross-polarized image of the same area as that in **Fig. 5a** captured with $\alpha_1 = 5°$ and a narrow pass filter with $\lambda = 498$ nm. The arrows in **Fig. 5a** indicate grain boundaries. Compared to **Fig. 5a**, the presence of grain boundaries can be easily confirmed in a cross-polarized image with high contrast.

CONCLUSIONS

In conclusion, we address the possibility of applying the method of orientation determination to other materials. The key characteristic is anisotropic extinction coefficient. Small organic molecules with aromatic rings in planar structures often crystalize in herringbone structure, which produces anisotropic optical properties. In fact, the anisotropic optical properties of organic molecules developed for organic electronics, such as DNTT, BTBT, dinaphtho[2,3-*b*:2′,3′-*d*]thiophene (DNT),[56] dinaphtho[2,3-*d*:2′,3′-*d*′]benzo[1,2-*b*:4,5-*b*′]dithiophene (DNBDT),[57] and its derivatives, have been observed by optical measurements.[2, 14–16, 21–26] The method is probably applicable to organic materials by adequately choosing the wavelength of irradiation light. Because organic materials with HOMO–LUMO energy gaps with less than ~2.7 eV absorb visible light, the crystal orientation might be determined by an optical microscope with a normal irradiation lamp. The candidate material includes pentacene, DNTT,[58–60] dianthra[2,3-*b*:2′,3′-*f*]thieno[3,2-*b*]thiophene (DATT),[10] 6,13-bis(triisopropylsilylethynyl)pentacene (TIPS-pentacene),[22, 25, 31, 32] and bis[1]benzothieno[2,3-*d*;2′,3′-*d*′]naphtho[2,3-*b*;6,7-*b*′]dithiophene (BBTNDT).[61] Actually, we observed a monolayer DNTT island, prepared for the demonstration, by PLM (**Fig. S8**). The luminance of reflected light from DNTT islands was very sensitive to α_1, as seen in **Fig. S8**. The result supports the abovementioned expectation.

Additionally, the orientation determination is probably useful for inorganic materials with anisotropic optical properties. For example, black phosphorus, which is a two-dimensional semiconductor with layered structure, has an in-plane anisotropic extinction coefficient in the

visible regime.[27–29] A periodic change in the color contrast similar to **Fig. 2d** has been observed for black phosphorus in PLM only with a polarizer,[27] though PLM with an analyzer was not applied.

In principle, the method of orientation determination is applicable to other ultra-thin materials (including organic and inorganic) with anisotropic extinction coefficient, as explained above. The described technique for quickly and easily imaging crystal axes using a standard optical microscope will help to understand the growth mechanism of thin films and the relationship between the microstructure and electrical properties in applications.

METHODS

Assignment of long and short axes The long and short axes of a cruciform DPh-DNTT island probably correspond to *b* and *a* axes of the crystal structure, respectively. Although few studies has been conducted on the anisotropic refractive index of DPh-DNTT, crystal axis determination is discussed by comparison with previous studies for other organic materials that have a similar molecular and crystal structure such as pentacene and DNTT, benzothieno[3,2-*b*][1]-benzothiophene (BTBT), and its derivative.[7–11] Previous studies on polarized absorption spectroscopy or PLM for a single-crystal film of pentacene, dioctyl-BTBT (C_8-BTBT) and 2-phenyl-7-hexyl-BTBT (Ph-BTBT-C_6), have indicated that films absorb light polarized in the *a* direction more than that in the *b* direction.[2, 15, 21] On other hand, pentacene islands with cruciform shapes have been formed by vacuum evaporation when the substrate is a single-crystal Si substrate, or when nucleation occurs on the first layer that forms on a thermally oxidized Si substrate.[17–19, 42, 43, 62, 63] In these studies, LEED and TSM micro-measurement revealed that the short axis corresponds to the *a* axis.[17, 18, 42] These findings suggest that the short and long axes of the monolayer island correspond to *a* and *b* axes, respectively. The suggestion is additionally supported by our density-functional theory calculations for the DPh-DNTT molecule (**Fig. S3**).

DPh-DNTT 2D islands Si wafer with a thermally grown SiO_2 film with a thickness of approximately 90 nm was used as a substrate, which is suitable for the visual detection of thin films. Monolayer DPh-DNTT islands were deposited on the substrate with a deposition rate of

0.05 Å/s at the pressure on the order of 10^{-4} Pa. The nominal thickness was monitored with a quartz crystal microbalance. The thickness of an island measured by AFM was ~2.3 nm,[49] which, is close to the length of DPh-DNTT molecule. DPh-DNTT molecules in a thin film deposited on a SiO_2/Si substrate stand nearly perpendicular to the substrate surface in herringbone packing structure.[8] The shape of the monolayer islands can be controlled by the substrate temperature during the deposition and the surface treatment of SiO_2 surface. Cruciform islands were formed on a substrate that was treated by an HF solution at 185°C. While round islands were formed on a substrate that was treated by UV-O_3 at 175°C. More details regarding the process are presented in our previous paper.[47, 49]

Microscopy observation Figure 1a shows the schematic diagram of the microscope (LV100, Nikon) equipped with a digital camera (EOS Kiss X4, Canon). Objective lenses [100×/NA = 0.9 (LU Plan 100×/0.9, Nikon) and 150×/NA = 0.9 (LU Plan Apo 150×/0.90, Nikon)] were used to acquire polarized and dark-field images, respectively. Two linear polarizers and a narrow band-pass filter were inserted in the optical path. The full width at half maximum of the narrow band-pass filters was approximately 35 nm. The polarizer for incident light was rotatable, and the analyzer for reflected light was fixed for all experiments. The transmission axes for the polarizer and the analyzer are represented as angles α_1 and α_2 with respect to the x-axis, respectively.

Optical model In Fig. 1e, E_i is the intensity of the polarized electrical field for incident light. The optical model [50, 51] consists of four materials: air, DPh-DNTT, SiO_2, and Si, numbered 0, 1, 2, and 3, respectively. d_1 is the thickness of the DPh-DNTT layer and was set to 2.3 nm.[8, 49] d_2 is the thickness of the SiO_2 layer, which was experimentally determined by spectroscopic ellipsometry and capacitance measurements. N_j (= $n_j + ik_j$; j = 0, 1, …, 3, i: imaginary unit) is a complex refractive index where the real part n_j is the phase velocity, and the imaginary part k_j indicates the amount of attenuation by absorption. Because Si and SiO_2 are optically isotropic materials, N_2 and N_3 are represented by certain values. On the other hand, N_1 for the DPh-DNTT layer is represented by N_{1L} for the long axis or N_{1S} for the short axis on the basis of the prediction that the DPh-DNTT island exhibits optical anisotropy. This prediction is supported by an earlier report that the optical properties of organic single crystals with a molecular structure similar to a DPh-DNTT molecule have anisotropy in a- and b-axes. Black arrow represents the optical path

for the electric field of light reflected on the SiO_2 surface; r_{sub} is the coefficient of reflection from the SiO_2 surface. Blue (red) arrow represents the optical path for the electric field polarized in the long (short) axis direction; r_L (r_S) is the reflection coefficient from a DPh-DNTT surface for the optical path. Reflection coefficient r_x (x = sub, L, or S) includes the influence of optical interference by multiple reflections illustrated with the arrow.

FIGURES

Figure 1 a, Inverted dark-filed optical microscope image of typical DPh-DNTT islands grown on a silicon substrate with a SiO_2 layer. **b,** Schematic illustration of a DPh-DNTT island to show the definition of θ, α_1, and α_2. The vertical and horizontal directions of the image are x and y, respectively. θ is the angle of the long axis with respect to the x-axis. α_1 and α_2 are the angles of transmission axes for the polarizer and analyzer. **c,** Chemical structure of the DPh-DNTT molecule and the top-view illustration of the herringbone structure. **d,** Schematic diagram of PLM. **e,** Schematic diagram of the light path in the cross section of the calculation model. Red and blue arrows represent the path of light parallel to long and short axes, respectively.

Figure 2 a, Dark-field optical microscope image of DPh-DNTT islands grown on a SiO_2/Si substrate treated with an HF solution captured without filters under unpolarized white light. Islands labeled with "a" and "b" have θ close to 0° and 90°, respectively. **b,** Bright-field image of the same area as the dark-field image observed under polarized 498-nm illumination without the analyzer; this image is obtained without any software modification. The arrow in the image indicates the transmission axis of the polarizer. **c,** Luminance contrast C_{exp} versus θ. The C_{exp} values for more than 170 islands are shown as closed circles. The solid line is a curve fitting of the closed circles obtained using **Eq. (3)**. The fitting curve has the maximum at θ = 0° and minimum at θ = 90°, which are represented as red and blue plots, respectively. **d,** C_{exp} values depending on wavelengths for θ = 0° (red closed circles) and 90° (blue closed circles). The solid line is a curve fitting of red or blue closed circles; it is obtained using N_{1L} = 1.45(±0.05) + 0.2i (±0.05i) or N_{1S} = 1.45(±0.05) + 0.4i (±0.05i), respectively.

Figure 3 Bright-field microscope images of DPh-DNTT islands. The images are captured at the same area as those in **Figs. 2a and 2b** and are acquired using the polarizer of $\alpha_1 = 5°$ (**a**), 0° (**b**), and −5° (**c**) and the analyzer without software modification. The double arrows, labeled with "P" and "A" in the images, indicate the transmission axes of the polarizer and the analyzer, respectively.

Figure 4 a, C_{exp} values for $\alpha_1 = 5°$ (red), 0° (black), and −5° (blue) depending on θ for **Fig. 3**. **b,** Experimental contrast as a function of α_1 for $\lambda = 498$ nm at $\theta = 45°$ (green closed circles) and 135° (orange closed circles). **c,** Contrast difference between $\theta = 45°$ and 135° as a function of λ for $\alpha_1 = -5°$. The vertical axis indicates orientation visibility.

Figure 5 Orientation mapping for round islands. a, Dark-field image with crystal axes. The red and blue lines indicate *a* and *b* axes, respectively. The arrows indicate grain boundaries. **b,** Bright-field cross-polarized image with $\alpha_1 = 5°$ observed by the illumination light of $\lambda = 498$ nm at the same area. The grain boundaries are clearly observed because of the contrast depending on the orientation.

SUPPORTING INFORMATION

Analytical solution of luminance contrast, image analysis, luminance contrast for various as a function of wavelength *N*, quantum chemical calculation of DPh-DNTT, color plot of the contrast as a function of λ and SiO_2 thickness, orientation determination for round monolayer islands, optical images change by rotating the sample, and optical images for monolayer islands of DNTT.

AUTHOR INFORMATION

*Corresponding Author

Email: hattori@eedept.kobe-u.ac.jp (Y. Hattori), kitamura@eedept.kobe-u.ac.jp (M. Kitamura)

ORCID

Yoshiaki Hattori: 0000-0002-5400-8820

Masatoshi Kitamura: 0000-0003-1342-4796

Notes

The authors declare no competing financial interests.

ACKNOWLEDGMENT

This work was partly supported by a Leading Initiative for Excellent Young Researchers program from the MEXT in Japan, JSPS KAKENHI Grant Numbers 19H02171, 19K15048, Materials Science Foundation from Hitachi Metals, Research Foundation for the Electrotechnology of Chubu, and Kawanishi Memorial ShinMaywa Education Foundation. The authors would like to thank Nippon Kayaku Co., Ltd. for supplying us DPh-DNTT.

REFERENCES

(1) Chu, T.; Liu, Y. A Theoretical Approach for Simulations of Anisotropic Charge Carrier Mobility in Organic Single Crystal Semiconductors. *Org. Electron.* **2018**, *53*, 165–184.

(2) Arai, S.; Inoue, S.; Hamai, T.; Kumai, R.; Hasegawa, T. Semiconductive Single Molecular Bilayers Realized Using Geometrical Frustration. *Adv. Mater.* **2018**, *30*, 1707256.

(3) Xie, W.; Willa, K.; Wu, Y.; Häusermann, R.; Takimiya, K.; Batlogg, B.; Frisbie, C. D. Temperature-Independent Transport in High-Mobility Dinaphtho-Thieno-Thiophene (DNTT) Single Crystal Transistors. *Adv. Mater.* **2013**, *25*, 3478–3484.

(4) Hofmockel, R.; Zschieschang, U.; Kraft, U.; Rödel, R.; Hansen, N. H.; Stolte, M.; Würthner, F.; Takimiya, K.; Kern, K.; Pflaum, J. High-Mobility Organic Thin-Film Transistors Based on a Small-Molecule Semiconductor Deposited in Vacuum and by Solution Shearing. *Org. Electron.* **2013**, *14*, 3213–3221.

(5) Ou-Yang, W.; Uemura, T.; Miyake, K.; Onish, S.; Kato, T.; Katayama, M.; Kang, M.; Takimiya, K.; Ikeda, M.; Kuwabara, H. High-Performance Organic Transistors with High-k Dielectrics: A Comparative Study on Solution-Processed Single Crystals and Vacuum-Deposited Polycrystalline Films of 2, 9-Didecyl-Dinaphtho [2, 3-b: 2′, 3′-f] Thieno [3, 2-b] Thiophene. *Appl. Phys. Lett.* **2012**, *101*, 223304.

(6) Jung, M.-C.; Leyden, M. R.; Nikiforov, G. O.; Lee, M. V.; Lee, H.-K.; Shin, T. J.; Takimiya, K.; Qi, Y. Flat-Lying Semiconductor–Insulator Interfacial Layer in DNTT Thin Films. *ACS Appl. Mater. Interfaces* **2015**, *7*, 1833–1840.

(7) Nabok, D.; Puschnig, P.; Ambrosch-Draxl, C.; Werzer, O.; Resel, R.; Smilgies, D.-M. Crystal and Electronic Structures of Pentacene Thin Films from Grazing-Incidence x-Ray Diffraction and First-Principles Calculations. *Phys. Rev. B* **2007**, *76*, 235322.

(8) Kang, M. J.; Miyazaki, E.; Osaka, I.; Takimiya, K.; Nakao, A. Diphenyl Derivatives of Dinaphtho [2, 3-b: 2′, 3′-f] Thieno [3, 2-b] Thiophene: Organic Semiconductors for Thermally Stable Thin-Film Transistors. *ACS Appl. Mater. Interfaces* **2013**, *5*, 2331–2336.

(9) Yamamoto, T.; Takimiya, K. Facile Synthesis of Highly π-Extended Heteroarenes, Dinaphtho [2, 3-b: 2 ‘, 3 ‘-f] Chalcogenopheno [3, 2-b] Chalcogenophenes, and Their Application to Field-Effect Transistors. *J. Am. Chem. Soc.* **2007**, *129*, 2224–2225.

(10) Niimi, K.; Shinamura, S.; Osaka, I.; Miyazaki, E.; Takimiya, K. Dianthra [2, 3-b: 2′, 3′-f] Thieno [3, 2-b] Thiophene (DATT): Synthesis, Characterization, and FET Characteristics of New π-Extended Heteroarene with Eight Fused Aromatic Rings. *J. Am. Chem. Soc.* **2011**, *133*, 8732–8739.

(11) Shinamura, S.; Osaka, I.; Miyazaki, E.; Nakao, A.; Yamagishi, M.; Takeya, J.; Takimiya, K. Linear-and Angular-Shaped Naphthodithiophenes: Selective Synthesis, Properties, and Application to Organic Field-Effect Transistors. *J. Am. Chem. Soc.* **2011**, *133*, 5024–5035.

(12) Huss-Hansen, M. K.; Hodas, M.; Mrkyvkova, N.; Hagara, J.; Jensen, B. B. E.; Osadnik, A.; Lützen, A.; Majková, E.; Siffalovic, P.; Schreiber, F.; Tavares, L.; Kjelstrup-Hansen, J.; Knaapila, M. Surface-Controlled Crystal Alignment of Naphthyl End-Capped Oligothiophene on Graphene: Thin-Film Growth Studied by in Situ X-Ray Diffraction. *Langmuir* **2020**, *36*, 1898–1906.

(13) Mannebach, E. M.; Spalenka, J. W.; Johnson, P. S.; Cai, Z.; Himpsel, F. J.; Evans, P. G. High Hole Mobility and Thickness-Dependent Crystal Structure in α,ω-Dihexylsexithiophene Single-Monolayer Field-Effect Transistors. *Adv. Funct. Mater.* **2013**, *23*, 554–564.

(14) Cheng, H.-L.; Mai, Y.-S.; Chou, W.-Y.; Chang, L.-R.; Liang, X.-W. Thickness-Dependent Structural Evolutions and Growth Models in Relation to Carrier Transport Properties in Polycrystalline Pentacene Thin Films. *Adv. Funct. Mater.* **2007**, *17*, 3639–3649.

(15) Minemawari, H.; Yamada, T.; Matsui, H.; Tsutsumi, J.; Haas, S.; Chiba, R.; Kumai, R.; Hasegawa, T. Inkjet Printing of Single-Crystal Films. *Nature* **2011**, *475*, 364–367.

(16) Storzer, T.; Hinderhofer, A.; Zeiser, C.; Novák, J.; Fišer, Z.; Belova, V.; Reisz, B.; Maiti, S.; Duva, G.; Hallani, R. K. Growth, Structure, and Anisotropic Optical Properties of Difluoro-Anthradithiophene Thin Films. *J. Phys. Chem. C* **2017**, *121*, 21011–21017.

(17) Sadowski, J. T.; Sazaki, G.; Nishikata, S.; Al-Mahboob, A.; Fujikawa, Y.; Nakajima, K.; Tromp, R. M.; Sakurai, T. Single-Nucleus Polycrystallization in Thin Film Epitaxial Growth. *Phys. Rev. Lett.* **2007**, *98*, 046104.

(18) Al-Mahboob, A.; Sadowski, J. T.; Fujikawa, Y.; Nakajima, K.; Sakurai, T. Kinetics-Driven Anisotropic Growth of Pentacene Thin Films. *Phys. Rev. B* **2008**, *77*, 035426.

(19) Al-Mahboob, A.; Fujikawa, Y.; Sakurai, T.; Sadowski, J. T. Real-Time Microscopy of Reorientation Driven Nucleation and Growth in Pentacene Thin Films on Silicon Dioxide. *Adv. Funct. Mater.* **2013**, *23*, 2653–2660.

(20) Fleming, A. J.; Netzer, F. P.; Ramsey, M. G. Nucleation and 3D Growth of Para-sexiphenyl Nanostructures from an Oriented 2D Liquid Layer Investigated by Photoemission Electron Microscopy. *J. Phys. Condens. Matter* **2009**, *21*, 445003.

(21) Yuan, Y.; Huang, J. Ultrahigh Gain, Low Noise, Ultraviolet Photodetectors with Highly Aligned Organic Crystals. *Adv. Opt. Mater.* **2016**, *4*, 264–270.

(22) James, D. T.; Frost, J. M.; Wade, J.; Nelson, J.; Kim, J.-S. Controlling Microstructure of Pentacene Derivatives by Solution Processing: Impact of Structural Anisotropy on Optoelectronic Properties. *ACS Nano* **2013**, *7*, 7983–7991.

(23) Fujikake, H.; Suzuki, T.; Isaka, F.; Sato, F. Orientation-Controlled Growth of Pentacene Single Crystal Films on an Alignment Layer Using Liquid Crystal as Solvent. *Jpn. J. Appl. Phys.* **2004**, *43*, L536.

(24) Cheng, H.-L.; Liang, X.-W.; Chou, W.-Y.; Mai, Y.-S.; Yang, C.-Y.; Chang, L.-R.; Tang, F.-C. Raman Spectroscopy Applied to Reveal Polycrystalline Grain Structures and Carrier Transport Properties of Organic Semiconductor Films: Application to Pentacene-Based Organic Transistors. *Org. Electron.* **2009**, *10*, 289–298.

(25) James, D. T.; Kjellander, B. C.; Smaal, W. T.; Gelinck, G. H.; Combe, C.; McCulloch, I.; Wilson, R.; Burroughes, J. H.; Bradley, D. D.; Kim, J.-S. Thin-Film Morphology of Inkjet-Printed Single-Droplet Organic Transistors Using Polarized Raman Spectroscopy: Effect of Blending TIPS-Pentacene with Insulating Polymer. *ACS Nano* **2011**, *5*, 9824–9835.

(26) Bhardwaj, B. S.; Sugiyama, T.; Namba, N.; Umakoshi, T.; Uemura, T.; Sekitani, T.; Verma, P. Raman Spectroscopic Studies of Dinaphthothienothiophene (DNTT). *Materials* **2019**, *12*, 615.

(27) Mao, N.; Tang, J.; Xie, L.; Wu, J.; Han, B.; Lin, J.; Deng, S.; Ji, W.; Xu, H.; Liu, K. Optical Anisotropy of Black Phosphorus in the Visible Regime. *J. Am. Chem. Soc.* **2016**, *138*, 300–305.

(28) Jiang, H.; Shi, H.; Sun, X.; Gao, B. Optical Anisotropy of Few-Layer Black Phosphorus Visualized by Scanning Polarization Modulation Microscopy. *ACS Photonics* **2018**, *5*, 2509–2515.

(29) Lan, S.; Rodrigues, S.; Kang, L.; Cai, W. Visualizing Optical Phase Anisotropy in Black Phosphorus. *ACS Photonics* **2016**, *3*, 1176–1181.

(30) Dai, F.; Liu, X.; Yang, T.; Qian, J.; Li, Y.; Gao, Y.; Xiong, P.; Ou, H.; Wu, J.; Kanehara, M.; Minari, M.; Liu, C. Fabrication of Two-Dimensional Crystalline Organic Films by Tilted Spin Coating for High-Performance Organic Field-Effect Transistors. *ACS Appl. Mater. Interfaces* **2019**, *11*, 7226–7234.

(31) Fesenko, P.; Rolin, C.; Janneck, R.; Bommanaboyena, S. P.; Gaethje, H.; Heremans, P.; Genoe, J. Determination of Crystal Orientation in Organic Thin Films Using Optical Microscopy. *Org. Electron.* **2016**, *37*, 100–107.

(32) Sharifzadeh, S.; Wong, C. Y.; Wu, H.; Cotts, B. L.; Kronik, L.; Ginsberg, N. S.; Neaton, J. B. Relating the Physical Structure and Optoelectronic Function of Crystalline TIPS-Pentacene. *Adv. Funct. Mater.* **2015**, *25*, 2038–2046.

(33) Yamamura, A.; Watanabe, S.; Uno, M.; Mitani, M.; Mitsui, C.; Tsurumi, J.; Isahaya, N.; Kanaoka, Y.; Okamoto, T.; Takeya, J. Wafer-Scale, Layer-Controlled Organic Single Crystals for High-Speed Circuit Operation. *Sci. Adv.* **2018**, *4*, eaao5758.

(34) He, D.; Zhang, Y.; Wu, Q.; Xu, R.; Nan, H.; Liu, J.; Yao, J.; Wang, Z.; Yuan, S.; Li, Y.; Shi, Y.; Wang, J.; Ni, Z.; He, L.; Miao, F.; Song, F.; Xu, H.; Watanabe, K.; Taniguchi, T.; Xu, J.-B.; Wang, X. Two-Dimensional Quasi-Freestanding Molecular Crystals for High-Performance Organic Field-Effect Transistors. *Nat. Commun.* **2014**, *5*, 1–7.

(35) Hamaguchi, A.; Negishi, T.; Kimura, Y.; Ikeda, Y.; Takimiya, K.; Bisri, S. Z.; Iwasa, Y.; Shiro, T. Single-Crystal-Like Organic Thin-Film Transistors Fabricated from Dinaphtho[2,3-*b*:2′,3′-*f*]Thieno[3,2-*b*]Thiophene (DNTT) Precursor-Polystyrene Blends. *Adv. Mater.* **2015**, *27*, 6606–6611.

(36) Kumatani, A.; Liu, C.; Li, Y.; Darmawan, P.; Takimiya, K.; Minari, T.; Tsukagoshi, K. Solution-Processed, Self-Organized Organic Single Crystal Arrays with Controlled Crystal Orientation. *Sci. Rep.* **2012**, *2*, 1–6.

(37) Li, Y.; Liu, C.; Kumatani, A.; Darmawan, P.; Minari, T.; Tsukagoshi, K. Large Plate-like Organic Crystals from Direct Spin-Coating for Solution-Processed Field-Effect Transistor Arrays with High Uniformity. *Org. Electron.* **2012**, *13*, 264–272.

(38) Inoue, S.; Shinamura, S.; Sadamitsu, Y.; Arai, S.; Horiuchi, S.; Yoneya, M.; Takimiya, K.; Hasegawa, T. Extended and Modulated Thienothiophenes for Thermally Durable and Solution-Processable Organic Semiconductors. *Chem. Mater.* **2018**, *30*, 5050–5060.

(39) Pérez-Rodríguez, A.; Temiño, I.; Ocal, C.; Mas-Torrent, M.; Barrena, E. Decoding the Vertical Phase Separation and Its Impact on C8-BTBT/PS Transistor Properties. *ACS Appl. Mater. Interfaces* **2018**, *10*, 7296–7303.

(40) Puntambekar, K.; Dong, J.; Haugstad, G.; Frisbie, C. D. Structural and Electrostatic Complexity at a Pentacene/Insulator Interface. *Adv. Funct. Mater.* **2006**, *16*, 879–884.

(41) Kalihari, V.; Tadmor, E. B.; Haugstad, G.; Frisbie, C. D. Grain Orientation Mapping of Polycrystalline Organic Semiconductor Films by Transverse Shear Microscopy. *Adv. Mater.* **2008**, *20*, 4033–4039.

(42) Kalihari, V.; Ellison, D. J.; Haugstad, G.; Frisbie, C. D. Observation of Unusual Homoepitaxy in Ultrathin Pentacene Films and Correlation with Surface Electrostatic Potential. *Adv. Mater.* **2009**, *21*, 3092–3098.

(43) Wu, Y.; Toccoli, T.; Zhang, J.; Koch, N.; Iacob, E.; Pallaoro, A.; Iannotta, S.; Rudolf, P. Key Role of Molecular Kinetic Energy in Early Stages of Pentacene Island Growth. *Appl. Phys. A* **2009**, *95*, 21–27.

(44) Sanda, S.; Nakamichi, R.; Nagase, T.; Kobayashi, T.; Takimiya, K.; Sadamitsu, Y.; Naito, H. Effect of Non-Chlorinated Solvents on the Enhancement of Field-Effect Mobility in Dioctylbenzothienobenzothiophene-Based Top-Gate Organic Transistors Processed by Spin Coating. *Org. Electron.* **2019**, *69*, 181–189.

(45) Kotsuki, K.; Tanaka, H.; Obata, S.; Stauss, S.; Terashima, K.; Saiki, K. The Importance of Spinning Speed in Fabrication of Spin-Coated Organic Thin Film Transistors: Film Morphology and Field Effect Mobility. *Appl. Phys. Lett.* **2014**, *104*, 233306.

(46) Mehta, S. B.; Shribak, M.; Oldenbourg, R. Polarized Light Imaging of Birefringence and Diattenuation at High Resolution and High Sensitivity. *J. Opt.* **2013**, *15*, 094007.

(47) Hattori, Y.; Kimura, Y.; Yoshioka, T.; Kitamura, M. The Growth Mechanism and Characterization of Few-Layer Diphenyl Dinaphthothienothiophene Films Prepared by Vacuum Deposition. *Org. Electron.* **2019**, *74*, 245–250.

(48) Hattori, Y.; Kimura, Y.; Yoshioka, T.; Kitamura, M. Data on Optical Microscopy and Vibrational Modes in Diphenyl Dinaphthothienothiophene Thin Films. *Data Brief* **2019**, *26*, 104522.

(49) Hattori, Y.; Kimura, Y.; Kitamura, M. Nucleation Density and Shape of Submonolayer Two-Dimensional Islands of Diphenyl Dinaphthothienothiophene in Vacuum Deposition. *J. Phys. Chem. C* **2020**, *124*, 1064–1069.

(50) Blake, P.; Hill, E. W.; Castro Neto, A. H.; Novoselov, K. S.; Jiang, D.; Yang, R.; Booth, T. J.; Geim, A. K. Making Graphene Visible. *Appl. Phys. Lett.* **2007**, *91*, 063124.

(51) Gorbachev, R. V.; Riaz, I.; Nair, R. R.; Jalil, R.; Britnell, L.; Belle, B. D.; Hill, E. W.; Novoselov, K. S.; Watanabe, K.; Taniguchi, T.; Geim, A. K.; Blake, P. Hunting for Monolayer Boron Nitride: Optical and Raman Signatures. *Small* **2011**, *7*, 465–468.

(52) Takimiya, K.; Osaka, I.; Mori, T.; Nakano, M. Organic Semiconductors Based on [1]Benzothieno[3,2-b][1]Benzothiophene Substructure. *Acc. Chem. Res.* **2014**, *47*, 1493–1502.

(53) Han, S.-H.; Yoo, S.; Kippelen, B.; Levi, D. Precise Determination of Optical Properties of Pentacene Thin Films Grown on Various Substrates: Gauss–Lorentz Model with Effective Medium Approach. *Appl. Phys. B* **2011**, *104*, 139–144.

(54) Park, S. P.; Kim, S. S.; Kim, J. H.; Whang, C. N.; Im, S. Optical and Luminescence Characteristics of Thermally Evaporated Pentacene Films on Si. *Appl. Phys. Lett.* **2002**, *80*, 2872–2874.

(55) Faltermeier, D.; Gompf, B.; Dressel, M.; Tripathi, A. K.; Pflaum, J. Optical Properties of Pentacene Thin Films and Single Crystals. *Phys. Rev. B* **2006**, *74*, 125416.

(56) Okamoto, T.; Mitsui, C.; Yamagishi, M.; Nakahara, K.; Soeda, J.; Hirose, Y.; Miwa, K.; Sato, H.; Yamano, A.; Matsushita, T.; Uemura, T.; Takeya, J. V-Shaped Organic Semiconductors With Solution Processability, High Mobility, and High Thermal Durability. *Adv. Mater.* **2013**, *25*, 6392–6397.

(57) Mitsui, C.; Okamoto, T.; Yamagishi, M.; Tsurumi, J.; Yoshimoto, K.; Nakahara, K.; Soeda, J.; Hirose, Y.; Sato, H.; Yamano, A.; Uemura, T.; Takeya, J. High-Performance Solution-Processable N-Shaped Organic Semiconducting Materials with Stabilized Crystal Phase. *Adv. Mater.* **2014**, *26*, 4546–4551.

(58) Milvich, J.; Zaki, T.; Aghamohammadi, M.; Rödel, R.; Kraft, U.; Klauk, H.; Burghartz, J. N. Flexible Low-Voltage Organic Phototransistors Based on Air-Stable Dinaphtho[2,3-b:2′,3′-f]Thieno[3,2-b]Thiophene (DNTT). *Org. Electron.* **2015**, *20*, 63–68.

(59) Chen, Y.; Chu, Y.; Wu, X.; Ou-Yang, W.; Huang, J. High-Performance Inorganic Perovskite Quantum Dot–Organic Semiconductor Hybrid Phototransistors. *Adv. Mater.* **2017**, *29*, 1704062.

(60) Kang, M. J.; Doi, I.; Mori, H.; Miyazaki, E.; Takimiya, K.; Ikeda, M.; Kuwabara, H. Alkylated Dinaphtho[2,3-b:2′,3′-f]Thieno[3,2-b]Thiophenes (Cn-DNTTs): Organic Semiconductors for High-Performance Thin-Film Transistors. *Adv. Mater.* **2011**, *23*, 1222–1225.

(61) Pei, K.; Ren, X.; Zhou, Z.; Zhang, Z.; Ji, X.; Chan, P. K. L. A High-Performance Optical Memory Array Based on Inhomogeneity of Organic Semiconductors. *Adv. Mater.* **2018**, *30*, 1706647.

(62) Meyer zu Heringdorf, F.-J.; Reuter, M. C.; Tromp, R. M. Growth Dynamics of Pentacene Thin Films. *Nature* **2001**, *412*, 517–520.

(63) Meyer zu Heringdorf, F.-J.; Reuter, M. C.; Tromp, R. M. The Nucleation of Pentacene Thin Films. *Appl. Phys. A* **2004**, *78*, 787–791.

Figure 1

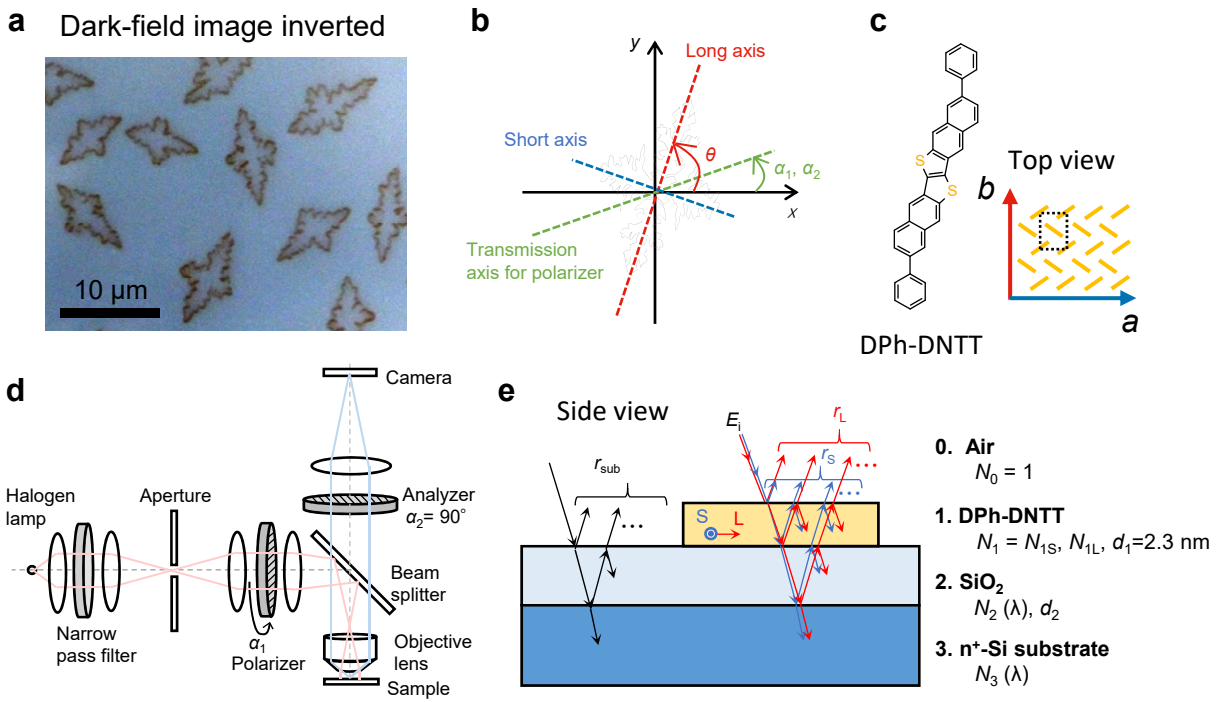
a
Dark-field image inverted
10 μm
b
Long axis
Short axis
θ
α1, α2
Transmission
axis for polarizer
y
x
c
Top view
b
a
DPh-DNTT
d
Camera
Halogen
lamp
Aperture
Analyzer
α2= 90°
Beam
splitter
Narrow
pass filter
α1
Polarizer
Objective
lens
Sample
e
Side view
Ei
rL
rS
rsub
S
L
0. Air
N0 = 1
1. DPh-DNTT
N1 = N1S, N1L, d1=2.3 nm
2. SiO2
N2 (λ), d2
3. n+-Si substrate
N3 (λ)

Figure 2

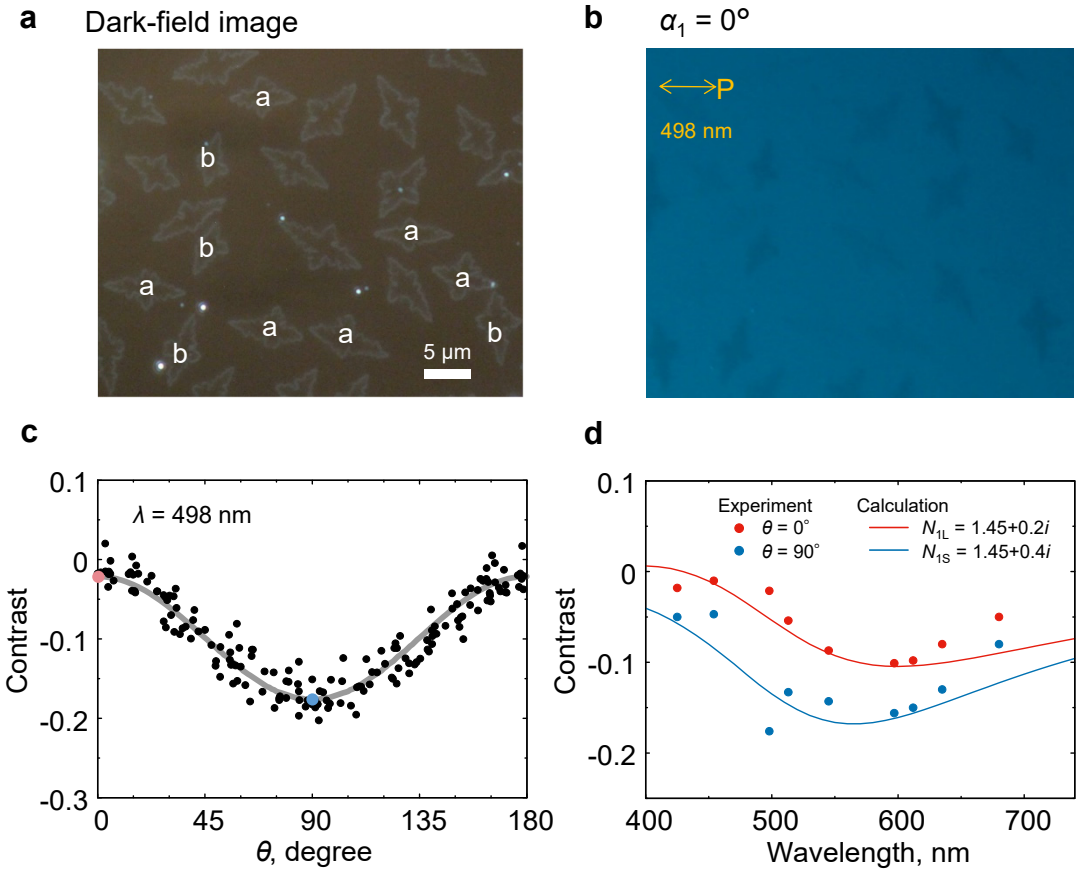
a
Dark-field image
a
b
b
a
a
a
a
a
b
b
5 μm
b
α_1 = 0°
P
498 nm
c
λ = 498 nm
Contrast
0.1
0
-0.1
-0.2
-0.3
0
45
90
135
180
θ, degree
d
Experiment
θ = 0°
θ = 90°
Calculation
N_{1L} = 1.45+0.2i
N_{1S} = 1.45+0.4i
Contrast
0.1
0
-0.1
-0.2
400
500
600
700
Wavelength, nm

Figure 3

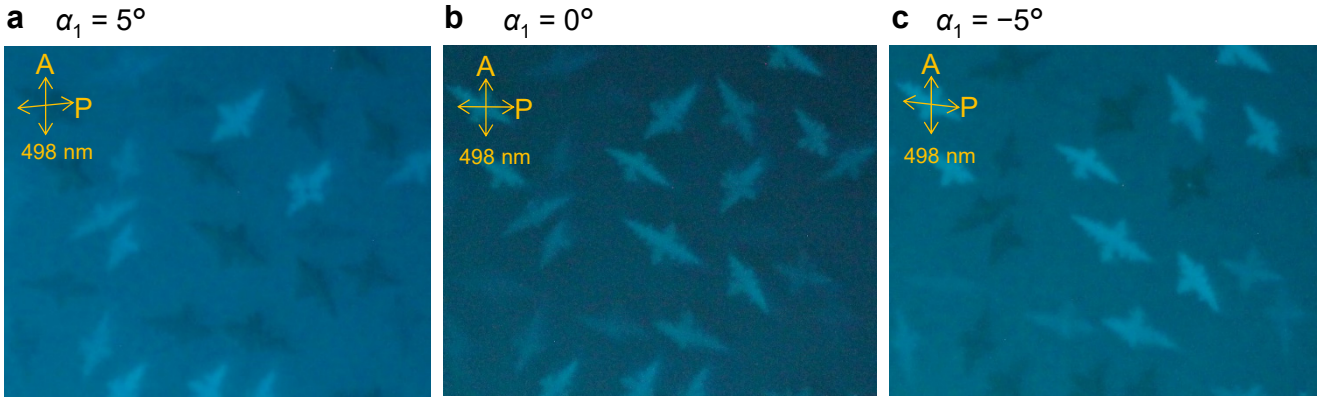

Figure 4

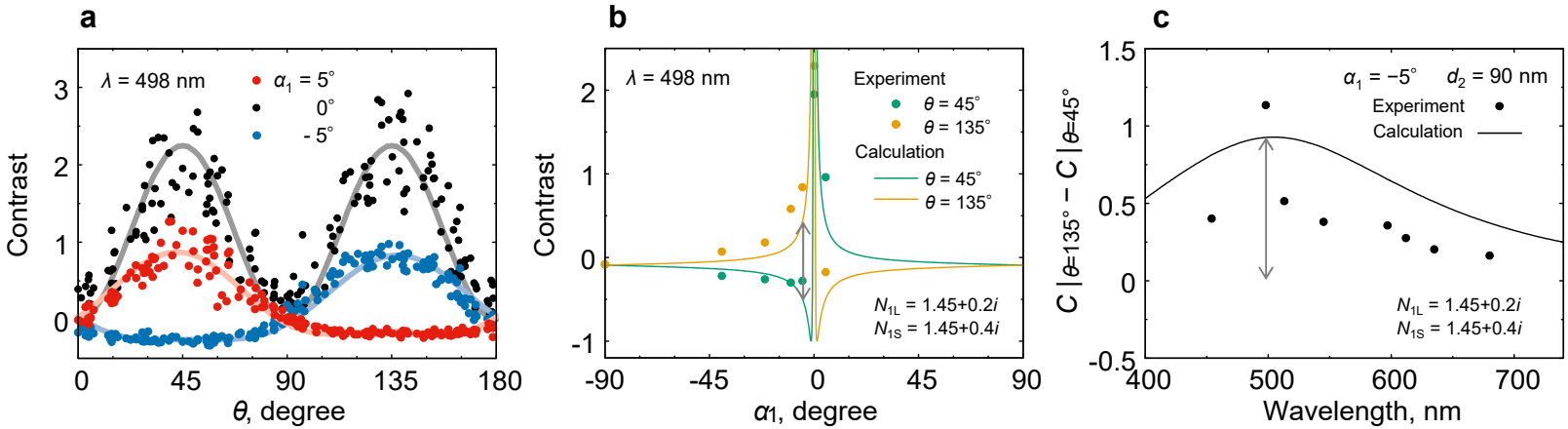
a
λ = 498 nm
α1 = 5°
0°
- 5°
Contrast
θ, degree
b
λ = 498 nm
Experiment
θ = 45°
θ = 135°
Calculation
θ = 45°
θ = 135°
N1L = 1.45+0.2i
N1S = 1.45+0.4i
Contrast
α1, degree
c
α1 = −5°
d2 = 90 nm
Experiment
Calculation
N1L = 1.45+0.2i
N1S = 1.45+0.4i
C |θ=135° − C |θ=45°
Wavelength, nm

Figure 5

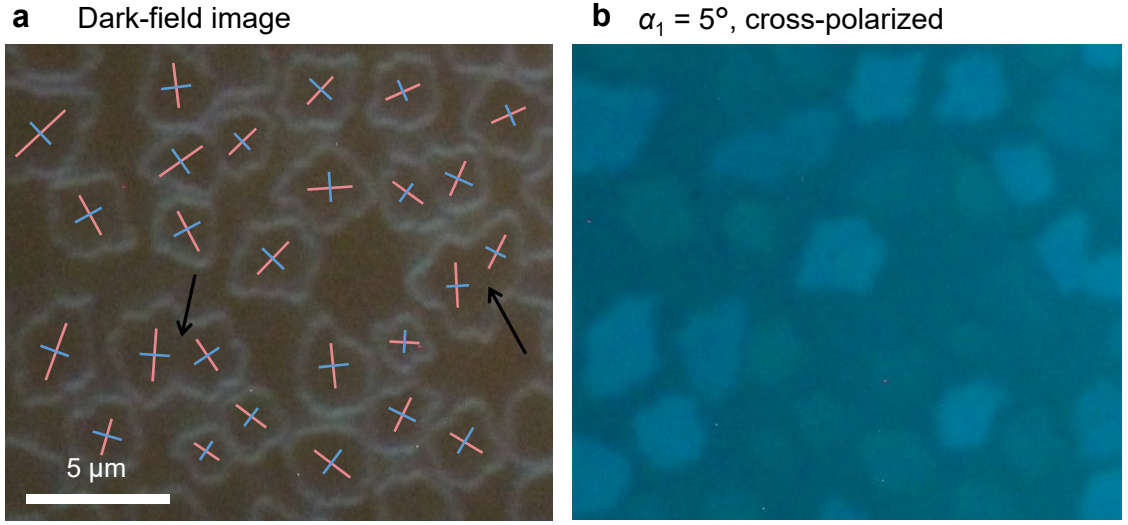

Supporting Information for:

Crystal orientation imaging of organic monolayer islands by polarized light microscopy

Yoshiaki Hattori[†*] *and Masatoshi Kitamura*[†*]

[†]Department of Electrical and Electronic Engineering, Kobe University, 1-1, Rokkodai-cho, Nada, Kobe, 657-8501, Japan

*Corresponding Author:
hattori@eedept.kobe-u.ac.jp (Y. Hattori), kitamura@eedept.kobe-u.ac.jp (M. Kitamura)

Contents:

1. Image analysis to determine luminance contrast

In this study, a microscope image captured using a digital camera is saved as 8-bit standard Red Green Blue (sRGB) data, which is used as a standard in monitors, printers, and digital cameras. Because luminance is nonlinearly converted to digital data in sRGB color, sRGB values at the pixel are converted to linear RGB values. Then, linear RGB values are transferred to (X, Y, Z) values in the XYZ color space with a reference to white illumination of D65/2°. The Y value is adopted as a value for the grayscale image. The contrast of an island with the SiO_2 surface, C_{exp}, is defined by **Eq. (1)**, which enables appropriate comparison even when contrast values are obtained at different irradiation intensities. The D_{DNTT} value for an island is the average at some pixels in the area of the island, and the D_{sub} value is the average at some pixels corresponding to the SiO_2 surface area surrounding the island.

Figure S1 shows polarized images in the same area obtained under illumination through band-pass filters of 454 nm (**a**), 498 nm (**b**), 597 nm (**c**), and 635 nm (**d**). The dotted lines in (**b**) represent long axes for cruciform islands with θ = 65° and 134°. **Figures S1 (e–h)** are grayscale images converted from **Figs. S1 (a–d)**. The yellow and blue bold lines in **Figs. S1 (e–h)** indicate areas that are adopted for the calculation of D_{DNTT} and D_{sub}, respectively. The values placed near the lines show D_{DNTT} and D_{sub} values used for the calculation of C_{exp} in **Eq. (1)**.

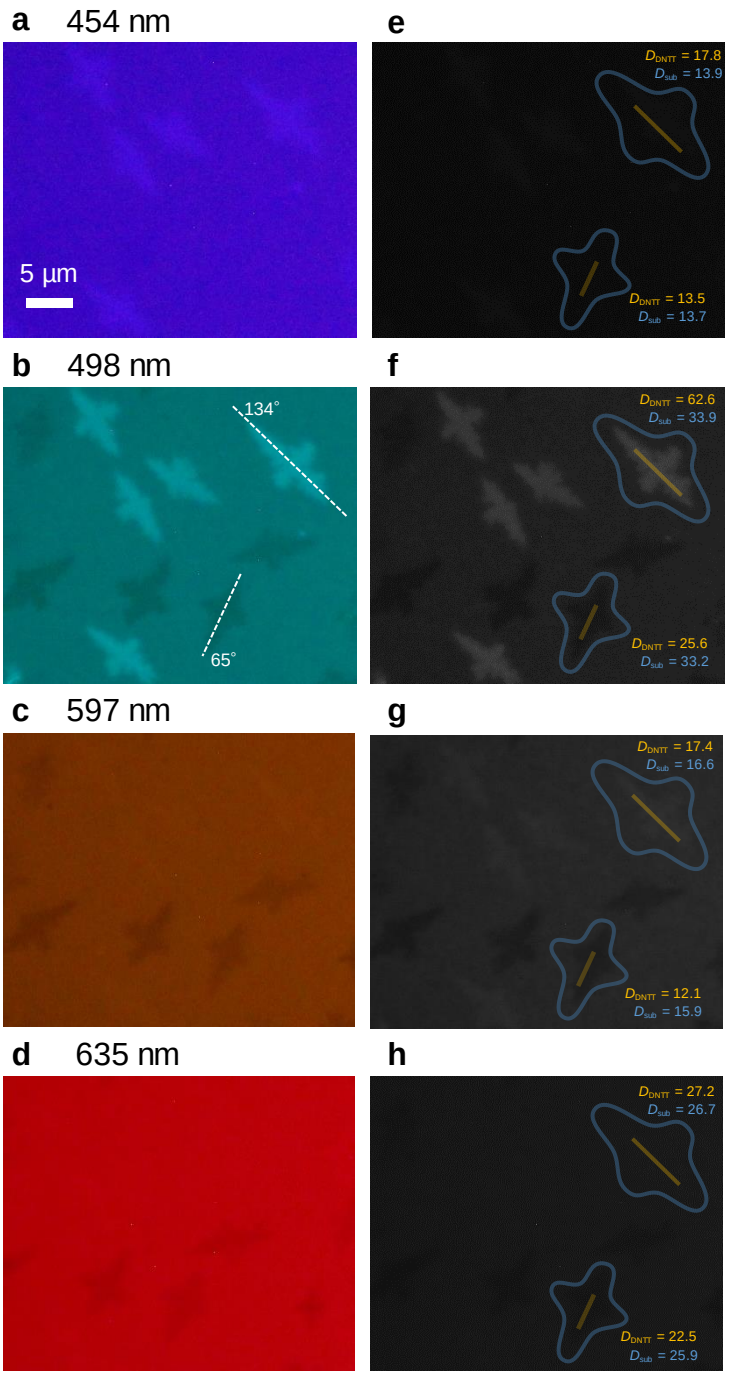

Figure S1: Original polarized images of DPh-DNTT islands and grayscale images obtained under illumination through band-pass filters of 454 nm (**a**), 498 nm (**b**), 597 nm (**c**), and 635 nm (**d**). (**e–h**) are grayscale images converted from (**a–d**).

2. Analytical solution of luminance contrast

2.1 Expression of light intensity

The luminance contrast of the image, C_{cal}, for islands is analytically derived on the basis of the Fresnel equation using Jones matrices. When light travels in the z direction, the intensity of light with electric field $\boldsymbol{E} = E_x \boldsymbol{e}_x + E_y \boldsymbol{e}_y$ is expressed as

$$I = \left|E_x\right|^2 + \left|E_y\right|^2 \tag{S1}$$

where $\boldsymbol{e}_x$ and $\boldsymbol{e}_y$ denote unit vectors in x and y directions, respectively. In this study, the electric fields for light reflected by the island and SiO_2 surfaces are respectively expressed as

$$\boldsymbol{E}_{\mathrm{DNTT}} = E_{x,\mathrm{DNTT}}\, \boldsymbol{e}_x + E_{y,\mathrm{DNTT}}\, \boldsymbol{e}_y, \tag{S2a}$$

$$\boldsymbol{E}_{\mathrm{sub}} = E_{x,\mathrm{sub}}\, \boldsymbol{e}_x + E_{\mathrm{y,sub}}\, \boldsymbol{e}_y. \tag{S2b}$$

Light intensities detected by an image sensor mounted on a microscope are denoted by I_{DNTT} for the island surface and I_{sub} for the SiO_2 surface.

2.2. Luminance contrast under polarized illumination

In this section, we derive the expression of luminance contrast under polarized illumination. Using Jones matrices

$$\boldsymbol{R}(\theta) = \begin{bmatrix} \cos\theta & \sin\theta \\ -\sin\theta & \cos\theta \end{bmatrix},$$

$$\boldsymbol{S}_{\mathrm{DNTT}} = \begin{bmatrix} r_{\mathrm{L}} & 0 \\ 0 & r_{\mathrm{S}} \end{bmatrix},$$

$$\boldsymbol{P} = \begin{bmatrix} 1 & 0 \\ 0 & 0 \end{bmatrix},$$

$\boldsymbol{E}_{\mathrm{DNTT}}$ is written as

$$\boldsymbol{E}_{\mathrm{DNTT}} = \boldsymbol{R}(-\theta)\boldsymbol{S}_{\mathrm{DNTT}}\boldsymbol{R}(\theta)\boldsymbol{R}(-\alpha_1)\boldsymbol{P}\boldsymbol{E}_{\mathrm{i}} \tag{S3}$$

where $\boldsymbol{E}_{\mathrm{i}}$ is the electric field of incident light and given by $E_{\mathrm{i}}\, \boldsymbol{e}_x + E_{\mathrm{i}}\, \boldsymbol{e}_y$. $\boldsymbol{R}(\theta)$, $\boldsymbol{S}_{\mathrm{DNTT}}$, and $\boldsymbol{P}$ serve as the rotation of angle θ, reflection by the island surface, and polarization in the x direction, respectively. For the elements of $\boldsymbol{S}_{\mathrm{DNTT}}$, r_{L} is the reflection coefficient for light for which the polarization is parallel to the long axis, and r_{S} is that for the short axis. Thus, $\boldsymbol{R}(-\alpha_1)\boldsymbol{P}\boldsymbol{E}_{\mathrm{i}}$ in **Eq. (S3)** represents light polarized in the direction of angle α_1. Similarly, $\boldsymbol{R}(-\theta)\boldsymbol{S}_{\mathrm{DNTT}}\boldsymbol{R}(\theta)$ serves as a reflection by island for which the long axis is in the direction of θ. This occurs because $\boldsymbol{S}_{\mathrm{DNTT}}$ is

defined as the reflection by island for which the long axis is in the x direction. Reflection coefficient r_X (X = S or L) by the island surface is written as

$$r_X = \frac{r_{01X} + r_{123X}\exp(i2\beta_{1X})}{1 + r_{01X}r_{123X}\exp(i2\beta_{1X})}, \tag{S4a}$$

$$r_{123X} = \frac{r_{12X} + r_{23}\exp(i2\beta_2)}{1 + r_{12X}r_{23}\exp(i2\beta_2)}, \tag{S4b}$$

$$r_{23} = \frac{N_3 - N_2}{N_3 + N_2}, \tag{S4c}$$

$$r_{12X} = \frac{N_2 - N_{1X}}{N_2 + N_{1X}}, \tag{S4d}$$

$$r_{01X} = \frac{N_{1X} - N_0}{N_{1X} + N_0}, \tag{S4e}$$

$$\beta_{1X} = \frac{2\pi d_1 N_{1X}}{\lambda}, \tag{S4f}$$

$$\beta_2 = \frac{2\pi d_2 N_2}{\lambda} \tag{S4g}$$

where λ is the wavelength of incident light. N_0, N_{1X}, N_2, and N_3 are refractive indices, as explained in main text.

On the other hand, using Jones matrices $\boldsymbol{R}(-\alpha_1)$, $\boldsymbol{P}$, and

$$\boldsymbol{S}_{sub} = \begin{bmatrix} r_{sub} & 0 \\ 0 & r_{sub} \end{bmatrix},$$

$\boldsymbol{E}_{sub}$ is written as

$$\boldsymbol{E}_{sub} = \boldsymbol{S}_{sub}\boldsymbol{R}(-\alpha_1)\boldsymbol{P}\boldsymbol{E}_i, \tag{S5}$$

where r_{sub} is the isotropic reflection coefficient by the SiO_2 surface. The expression of r_{sub} is obtained by substituting $d_1 = 0$ in **Eq. (S4f)**.

Using **Eqs. (S3) and (S5)**, I_{DNTT} and I_{sub} are written as

$$I_{DNTT} = \frac{E_i^2}{2}\left\{\left(|r_L|^2 - |r_S|^2\right)\cos\left(2\theta - 2\alpha_1\right) + \left(|r_L|^2 + |r_S|^2\right)\right\}, \tag{S6}$$

and

$$I_{sub} = E_i^2 |r_{sub}|^2, \tag{S7}$$

respectively. By substituting **Eqs. (S6) and (S7)** into **Eq. (2)**, we obtain

$$C_{\mathrm{cal}} = A_1 \cos\left(2\theta - 2\alpha_1\right) + A_2 \tag{S8}$$

as luminance contrast under polarized illumination, where $A_1 = \frac{1}{2}\left(\left|\frac{r_{\mathrm{L}}}{r_{\mathrm{sub}}}\right|^2 - \left|\frac{r_{\mathrm{S}}}{r_{\mathrm{sub}}}\right|^2\right)$ and $A_2 = \frac{1}{2}\left(\left|\frac{r_{\mathrm{L}}}{r_{\mathrm{sub}}}\right|^2 + \left|\frac{r_{\mathrm{S}}}{r_{\mathrm{sub}}}\right|^2 - 2\right)$ are real constants. Of note, C_{cal} does not depend on θ when an organic island has an isotropic reflection coefficient so that $r_{\mathrm{L}} = r_{\mathrm{S}}$. In this case, the islands have the same contrast independent of θ.

2.3. Analysis of the observation with crossed polarizers

In this section, we derive expressions of C_{cal} and I_{DNTT} for the observation with crossed polarizers. Because light reflected by the substrate surface passes through an analyzer, $\boldsymbol{E}_{\mathrm{DNTT}}$ and $\boldsymbol{E}_{\mathrm{sub}}$ are expressed as

$$\boldsymbol{E}_{\mathrm{DNTT}} = \boldsymbol{R}(-\alpha_2)\boldsymbol{P}\boldsymbol{R}(\alpha_2)\boldsymbol{R}(-\theta)\boldsymbol{S}_{\mathrm{DNTT}}\boldsymbol{R}(\theta)\boldsymbol{R}(-\alpha_1)\boldsymbol{P}\boldsymbol{E}_{\mathrm{i}} \tag{S9}$$

and

$$\boldsymbol{E}_{\mathrm{sub}} = \boldsymbol{R}(-\alpha_2)\boldsymbol{P}\boldsymbol{R}(\alpha_2)\boldsymbol{S}_{\mathrm{sub}}\boldsymbol{R}(-\alpha_1)\boldsymbol{P}\boldsymbol{E}_{\mathrm{i}}, \tag{S10}$$

respectively. $\boldsymbol{R}(-\alpha_2)\boldsymbol{P}\boldsymbol{R}(\alpha_2)$ serves as an analyzer of angle α_2. In this study, α_2 was fixed at 90°. Thus, by substituting $\alpha_2 = 90°$ in **Eqs. (S9) and (S10)**, I_{DNTT} and I_{sub} are, respectively, written as

$$I_{\mathrm{DNTT}} = E_{\mathrm{i}}^2 \left| r_{\mathrm{L}} \sin\theta\cos\left(\theta - \alpha_1\right) - r_{\mathrm{S}} \cos\theta \sin\left(\theta - \alpha_1\right)\right|^2, \tag{S11}$$

$$I_{\mathrm{sub}} = E_{\mathrm{i}}^2 \left| r_{\mathrm{sub}} \right|^2 \sin^2(\alpha_1). \tag{S12}.$$

When α_1 is zero, I_{sub} is equal to zero, and **Eq. (2)** for C_{cal} cannot be used to evaluate color contrast. Therefore, light reflection is evaluated in the following cases.

(i) $\alpha_1 \neq 0°$

In this case, **Eq. (2)** for C_{cal} can be used to evaluate luminance contrast. By substituting **Eqs. (S11) and (S12)** into **Eq. (2)**, C_{cal} is written as

$$C_{\mathrm{cal}} = B_1\left(\frac{\sin\theta\cos(\theta-\alpha_1)}{\sin\alpha_1}\right)^2 + B_2\left(\frac{\cos\theta\sin(\theta-\alpha_1)}{\sin\alpha_1}\right)^2 - B_3\left(\frac{\sin\theta\cos(\theta-\alpha_1)}{\sin\alpha_1}\right)\left(\frac{\cos\theta\sin(\theta-\alpha_1)}{\sin\alpha_1}\right) - 1$$

(S13),

where $B_1 = |r_L|^2$, $B_2 = |r_S|^2$, and $B_3 = r_L r_S^* + r_L^* r_S$ are real constants. C_{cal} is a function of θ with a period of 180°. When N_{1S} and N_{1L} are known, C_{cal} can be calculated using the geometric and experimental parameters.

(ii) $\alpha_1 = 0°$

In this case, **Eq. (S11)** for I_{DNTT} is used to evaluate light reflected by the island surface. By substituting $\alpha_1 = 0°$ into **Eq. (S11)**, I_{DNTT} is written as

$$I_{\mathrm{DNTT}} = F\left(1-\cos 4\theta\right) \qquad \text{(S14)}$$

where $F = \frac{E_i^2}{8}\left|r_L - r_S\right|^2$ is the real constant. I_{DNTT} is a function of θ with a period of 90°. The period for I_{DNTT} is consistent with the dependence of contrast on θ for $\alpha_1 = 0°$ shown in **Fig. 4a**.

3. Supporting figures

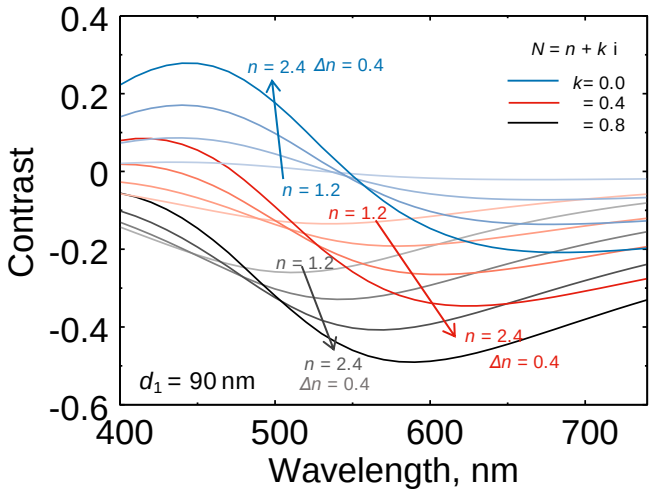

Figure S2: Luminance contrast C_{cal} calculated as a function of wavelength for different N (= N_{1L} = N_{1S}) using **Eq. (3a)** under $\theta = 0$ or 90°. The change in C_{cal} is sensitive to n and k. Thus, n and k can be independently determined by fitting a curve obtained from **Eq. (3a)** to experimental C_{exp} values as a function of wavelength.

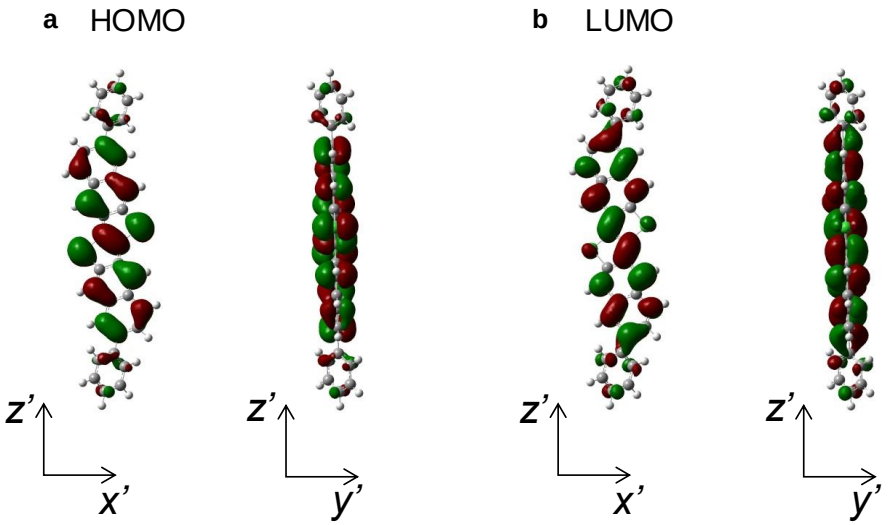

Figure S3: Molecular orbitals of HOMO **(a)** and LUMO **(b)** for DPh-DNTT obtained by the quantum chemical calculation. The molecular orbital of HOMO has low symmetry in the x' direction, high asymmetry in the y' direction, and low symmetry in the z' direction. While the molecular orbital of LUMO has low symmetry in the x' direction, high asymmetry in the y' direction, and low asymmetry in the z' direction. The consideration of transition probability suggests that the DPh-DNTT molecule absorbs more light polarized in the x' direction than in the y' direction. The consideration is consistent with the experiment.

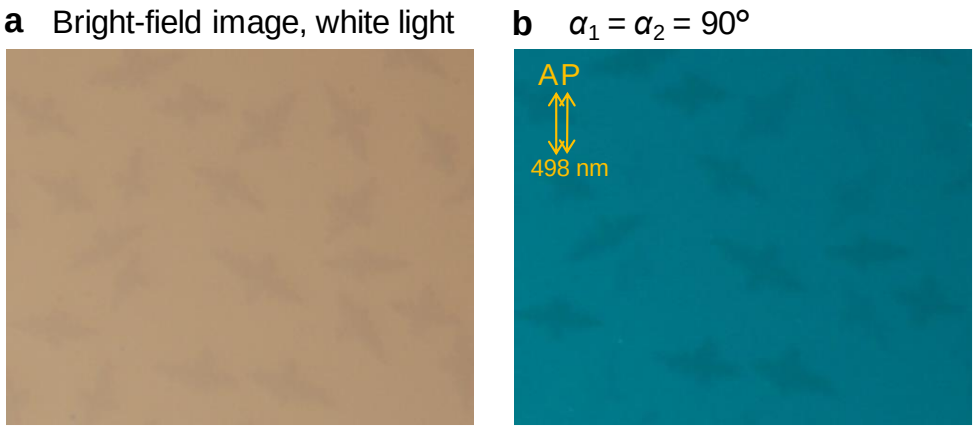

Figure S4: **a,** Bright-filed microscope image observed in the same area as those in **Figs. 2a** and **2b** under unpolarized white illumination. **b,** Bright-field image observed under illumination through band-pass filters of 498 nm with two polarizers at $\alpha_1 = \alpha_2 = 90°$. In this case, islands that have θ close to 0° appear darker than the surrounding area. This result corresponds to the polarized optical image captured using only polarizer for $\alpha_1 = 90°$, which is comparable to **Fig. 2b**.

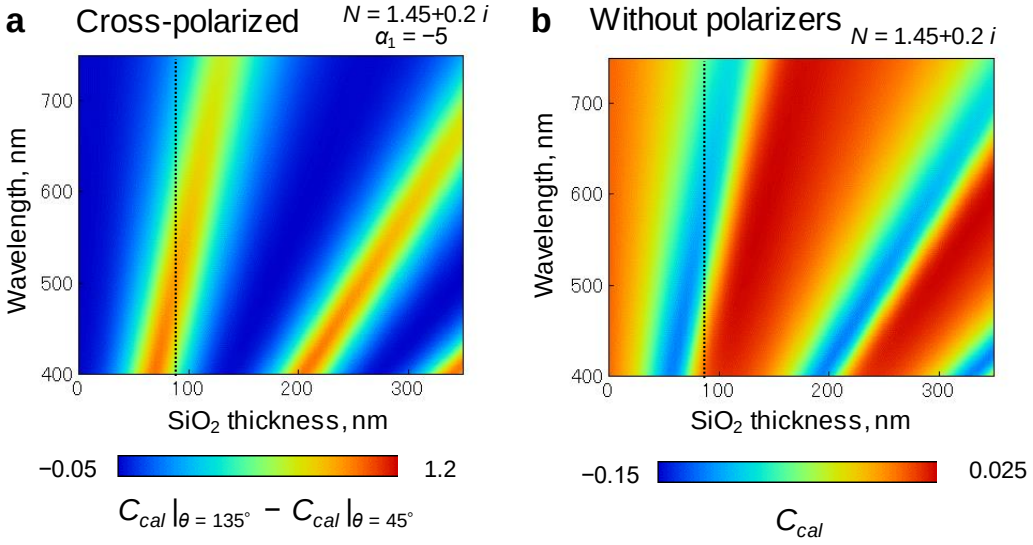

Figure S5: **a,** Color plot of the contrast difference between $\theta = 45°$ and 135° as a function of λ and SiO_2 thickness (d_2) in crossed-polarized observation at $\alpha_1 = -5°$. The color scale at the bottom shows the calculated contrast. The dotted line in the figure corresponds to **Fig. 4c**. The combination of λ and d_2 for the red region is suitable for domain orientation imaging. **b,** Color plot of the contrast as a function of λ and SiO_2 thickness in the observation without polarizers. The dotted line in the figure corresponds to **Fig. 2d**. The combination of λ and d_2 for the blue region is suitable for imaging thin films on SiO_2.

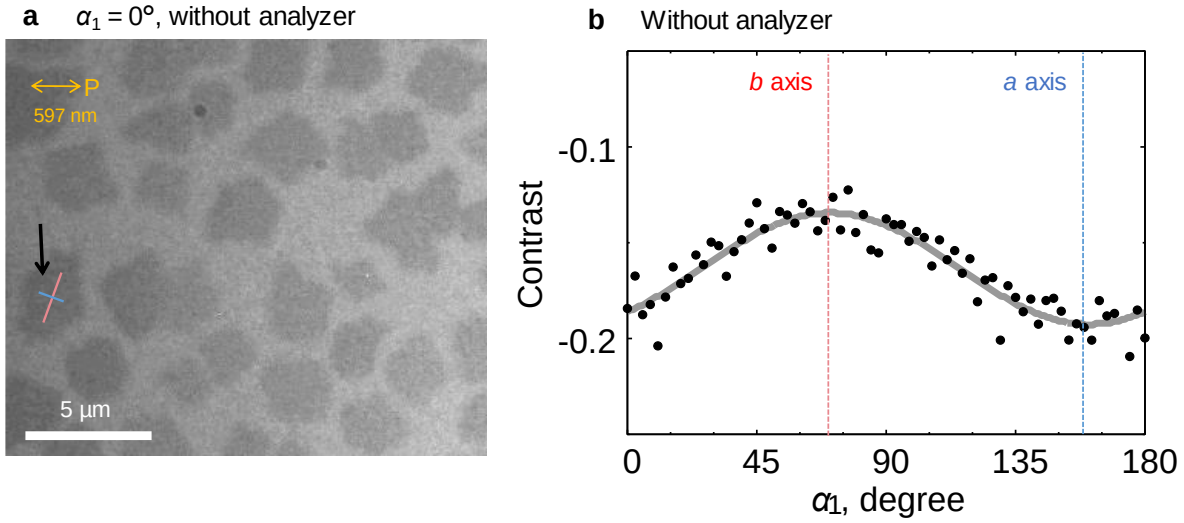

Figure S6: Orientation determination by changing α_1 in the observation by polarized illumination without an analyzer. Multiple photos are acquired by rotating the polarizer. **a,** Grayscale image obtained by polarized 597 nm illumination at $\alpha_1 = 0°$. The angle dependence of the polarizer is examined. **b,** The angle dependence of the island in **a** indicated by an arrow. The dependence is a trigonometric function in the double periodic change. It is expected from **Eq. (3b)**. From the top and bottom peak, the crystal axes are determined, which are indicated in **a** by red and blue lines.

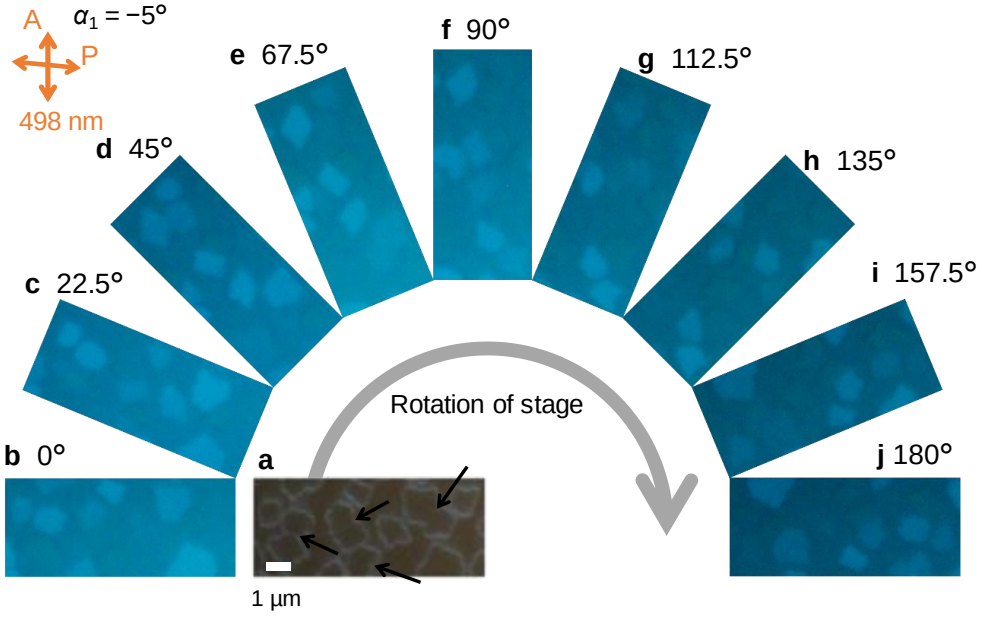

Figure S7: Optical images change by rotating the sample during cross-polarized observation at $\alpha_1 = -5°$. **a,** Dark-field image. The arrows indicate the grain boundaries. **b–j,** Cross-polarized images at the same area obtained by rotating the sample stage. The color change in the double periodic change is observed. The change allows to determine the grain orientation.

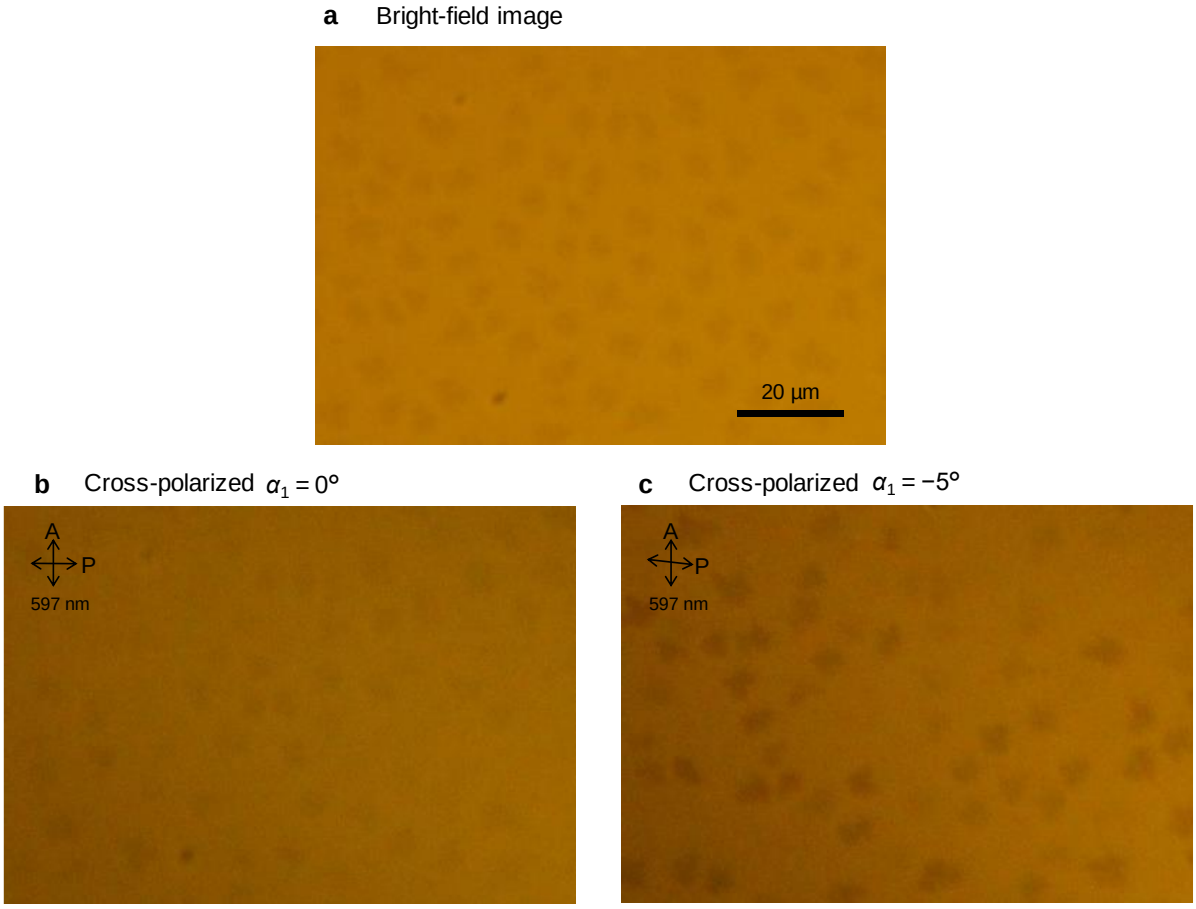

Figure S8: Optical images for sub-monolayer DNTT on a thermally grown Si substrate with a thickness of 90 nm. DNTT thin films were deposited at the pressure on the order of 10^{-4} Pa with a deposition rate of 0.05 Å/s at the substrate temperature of 70°C. **a,** Bright-field image observed by 597-nm illumination without polarizers. **b,** Crossed-polarized image at $\alpha_1 = 0°$. **c,** Crossed-polarized image at $\alpha_1 = -5°$. Color split is observed, which suggests that DNTT islands have an anisotropic extinction coefficient.